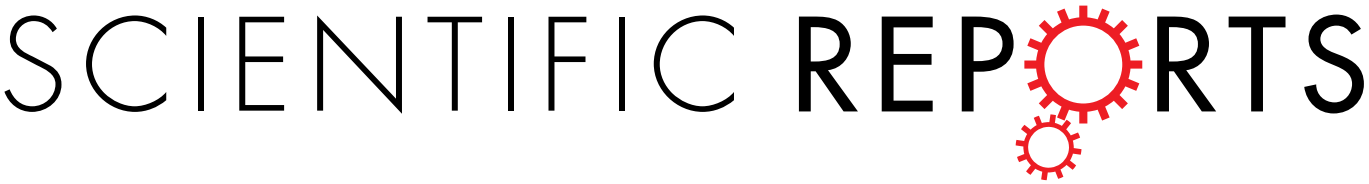

OPEN

High-responsivity UV-Vis Photodetector Based on Transferable WS_2 Film Deposited by Magnetron Sputtering

Received: 14 October 2015
Accepted: 30 December 2015
Published: 29 January 2016

Longhui Zeng*, Lili Tao*, Chunyin Tang, Bo Zhou, Hui Long, Yang Chai, Shu Ping Lau & Yuen Hong Tsang

The two-dimensional layered semiconducting tungsten disulfide (WS_2) film exhibits great promising prospects in the photoelectrical applications because of its unique photoelectrical conversion property. Herein, in this paper, we report the simple and scalable fabrication of homogeneous, large-size and transferable WS_2 films with tens-of-nanometers thickness through magnetron sputtering and post annealing process. The produced WS_2 films with low resistance (4.2 kΩ) are used to fabricate broadband sensitive photodetectors in the ultraviolet to visible region. The photodetectors exhibit excellent photoresponse properties, with a high responsivity of 53.3 A/W and a high detectivity of 1.22×10^{11} Jones at 365 nm. The strategy reported paves new way towards the large scale growth of transferable high quality, uniform WS_2 films for various important applications including high performance photodetectors, solar cell, photoelectrochemical cell and so on.

The successful isolation of graphene from graphite has attracted extensive amounts of attention due to its attractive electrical and mechanical properties[1,2], and its great potentials in advanced electronic and photonic applications[3–8]. However, the zero bandgap of graphene limits its application in optoelectronics. Recently, the emergence of two-dimensional (2D) graphene-like transition metal dichalcogenides (TMDs) have very well remedied the zero-bandgap disadvantage and attracted tremendous attention due to its semiconducting properties and potential for various optical, electrical and photoelectrical applications[9–12]. WS_2 and MoS_2 are the two most typical TMDs with layered structure constructed of S-W/Mo-S atomic tri-layer units[13,14]. Compared with MoS_2, WS_2 has higher thermal stability and wider operational temperature range[15], possessing a controllable bandgap ranging from 1.4 to 2.1 eV depending on the proper layer structure[11,16], leading to a broad UV to Visible (UV-Vis) absorption band. Furthermore, WS_2 has been reported to have strong absorbance as high as 5~10% of incident sunlight in the thickness of ~1 nm, one order of magnitude higher than GaAs and Si[17], showing great potential for photocatalysis, solar cells and high-responsivity UV-Vis photodetector applications.

Preparation of uniform large area WS_2 thin film is the most fundamental step for various device fabrications. WS_2 films can be prepared through top-down or bottom-up methods. Top-down method through mechanical or chemical exfoliation from the bulk crystals form have difficulty to control the size and thickness and obtain uniform WS_2 films[18–20]. Among the bottom-up methods, chemical vapor deposition (CVD) can commonly produce large-area single-crystal 2D films, such as monolayer graphene[21], however for TMDs (MoS_2, WS_2), there has been no reports on the preparation of wafer scale single-crystal films through CVD method yet, except for the preparation of micrometer sized triangular MoS_2 and WS_2[22–24]. As for the preparation of polycrystalline TMD films, the magnetron sputtering deposition method has proved to be better than the CVD method because of its simplicity, low cost, high production speed and scalability.

In this work, a facial and scalable magnetron sputtering method was employed to fabricate the transferable continuous centimeter sized polycrystalline WS_2 film with thickness of ~25.2 nm, which is then used to produce high performance UV-Vis photodetectors, showing excellent photo-response properties from the ultraviolet to

Department of Applied Physics, The Hong Kong Polytechnic University, Hung Hom, Kowloon, Hong Kong. *These authors contributed equally to this work. Correspondence and requests for materials should be addressed to Y.H.T. (email: yuen.tsang@polyu.edu.hk)

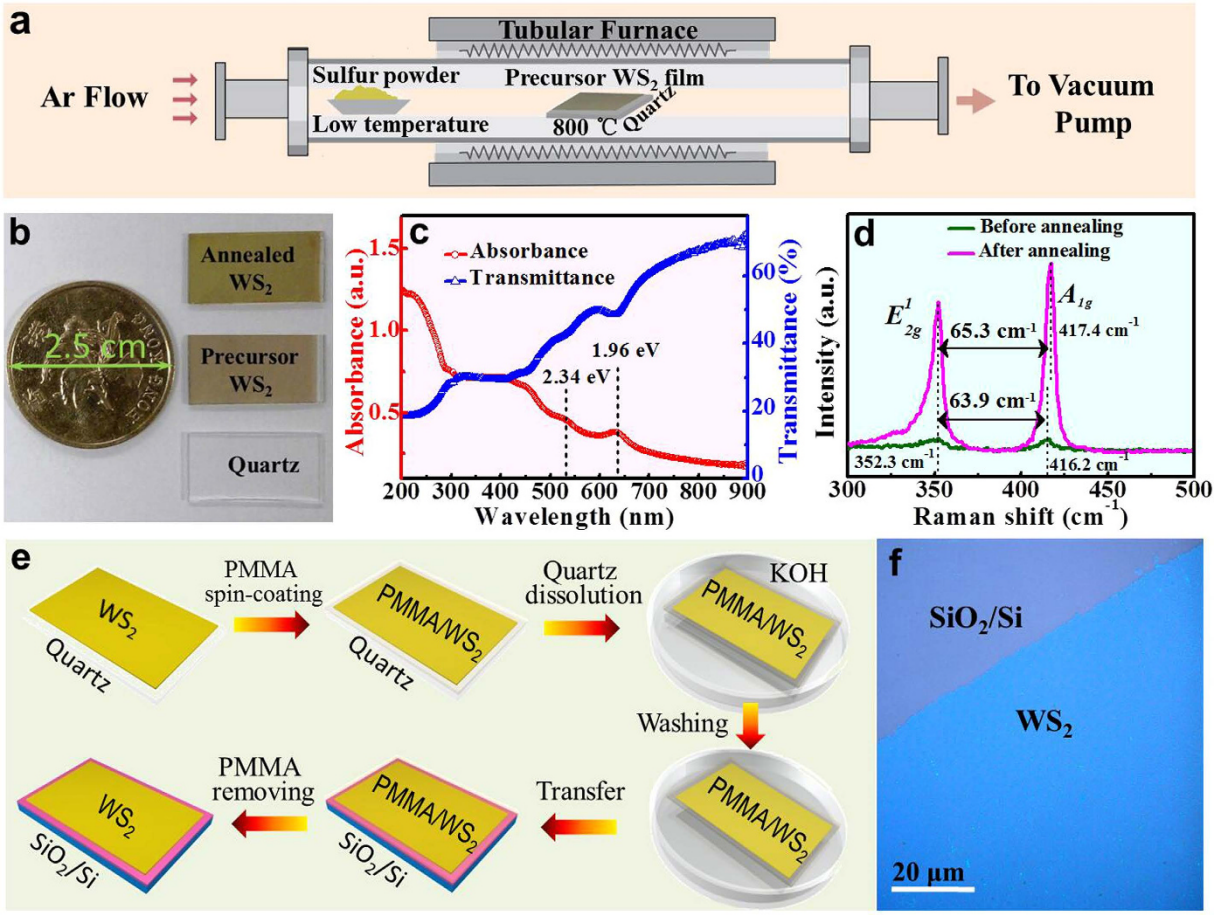

Figure 1. Preparation and transfer of WS_2 film. (**a**) Schematic diagram of the annealing process for WS_2 films. (**b**) A photograph of quartz and WS_2 on quartz before and after annealing. (**c**) Measured UV-Vis absorption and transmission spectra of the annealed WS_2 films. (**d**) Raman spectra of WS_2 films before and after annealing. (**e**) Scheme of the transferring process of grown WS_2 film from Quartz to SiO_2/Si substrate. (**f**) Optical image of the transferred WS_2 film on SiO_2/Si substrate.

visible region (365–650 nm), such as high responsivity (53.3 A/W), high detectivity (up to $\approx 10^{11}$ Jones) at 365 nm. Therefore it is expected that this transferable high quality large-area WS_2 films has great potential applications in not only photodetectors but also other photoelectrical functional devices.

Results

WS_2 films on quartz substrate were produced by magnetron sputtering followed by post annealing. A WS_2 precursor film was first deposited on clean quartz substrate through sputtering by using a sintered WS_2 disk as the target. The post annealing process was then carried out to enhance the crystallinity of the WS_2 film. Figure 1a shows the schematic diagram of the annealing process, the WS_2 precursor film on quartz was loaded in a tubular reactor, and sulfur powder was placed upstream into the chamber. Sulfur was evaporated at 200 °C and dragged by Argon flow, and the center temperature of the tube furnace was set to 800 °C and kept for 2 hours, followed by cooling down to room temperature naturally to complete the annealing processes. Figure 1b shows the photographs of bare quartz, the WS_2 precursor film and annealed film on the quartz substrates used for this experiment and their relative size as a one dollar coin from Hong Kong of 2.5 cm diameter. The gray sputtered WS_2 precursor film shows a characteristic yellowish green color of few-layer WS_2 crystal after annealing.

In Fig. 1c, the optical absorption and transmittance spectra of the annealed WS_2 film are presented. Generally, the WS_2 film possesses considerable photo-absorption covering the entire UV-Vis range of 200–900 nm, demonstrating the very broad ultraviolet to visible range photoelectrical response from the fabricated WS_2 film based photodetector. Figure 1c records two characteristic absorption peaks at 633 nm (1.96 eV) and 530 nm (2.34 eV) arising from direct transition from valance band to conduction band at the K-point of the Brillouin zone, known as the A and B transitions, respectively. The two peaks formed due to the spin-orbital splitting of the valence band. In addition, the characteristic C peak centered at 455 nm (2.72 eV) is also observed[25,26]. As is well known that, the bandgap becomes smaller for the thicker WS_2[16], all the three peaks have exhibited a little red shift compared with the mono- and bi-layer WS_2 reported, indicating the few-layer thickness of WS_2 obtained here[26].

The Raman spectra of theWS_2 films before and after annealing under 488 nm excitation were obtained and presented in Fig. 1d. The two characteristic peaks corresponding to the E^1_{2g} mode, in-plane vibration of tungsten

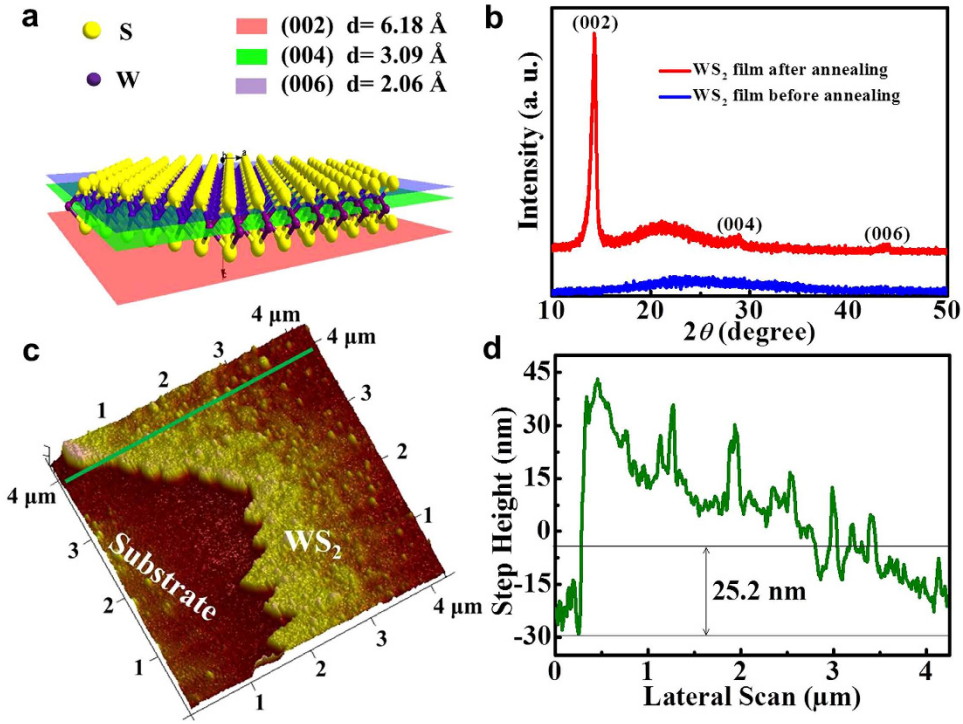

Figure 2. Characterization of WS_2 film. (**a**) Three-dimensional atomic structure diagram of monolayer WS_2. (**b**) XRD profile of WS_2 films on the quartz before and after annealing. (**c**) Three dimensional AFM image of annealed WS_2 film. (**d**) Height profile along the line marked in (**c**).

and sulfur atoms, and A_{1g} modes, the out-of-plane vibrations of the sulfur atoms, are observed from the both two films[27]. The Raman peaks are identified at 352.3 and 417.4 cm^{-1} for annealed WS_2 films, and 352.3 and 416.2 cm^{-1} for precursor WS_2 films, very close to the reported result of few-layered WS_2[10], the frequency difference of the two Raman peaks of the annealed WS_2 film is 65.1 cm^{-1}, indicating the film is made up of a few layered WS_2 nanostructure. The peak intensity of annealed WS_2 film is much stronger compared with the pre-annealed WS_2 film, which are contributed to the improvement of crystallinity resulting in strengthened lattice dynamics. Another unique feature observed in the Raman spectra is that the intensity ratio of A_{1g}/E^1_{2g} of the WS_2 film increased from ~0.97 to ~1.24 after annealing, and the A_{1g} peak of the WS_2 film slightly shifted to higher frequency while E^1_{2g} peak remained the same after annealing, indicating A_{1g} mode which represents the out-of-plane vibrations of the sulfur atoms has become more sensitive to post annealing process.

Figure 1e shows that the WS_2 films growth on the quartz can be transferred to other substrates such as SiO_2/Si for device fabrication. First, PMMA was spin-coated on the WS_2/quartz sample, followed by being immersed in potassium hydroxide (KOH) solution at 80 °C. KOH can etch the quartz substrate and then the PMMA/WS_2 film will float on the solution surface. The floating PMMA/WS_2 film was then washed with DI water for several times before being transferred to the new SiO_2/Si substrate and dried. Then the PMMA was finally dissolved in acetone. The optical image of the transferred WS_2 film on SiO_2/Si shown in Fig. 1f indicates the WS_2 film kept flat continuous after being transferred.

X-ray diffraction (XRD) method was carried out to investigate the crystalline structure and the composition of the WS_2 films. It is well known that each single plane of WS_2 comprises a tri-layer composed of a tungsten layer sandwiched between two sulfur layers as shown in Fig. 2a, with the (002), (004) and (006) crystal planes along the c direction being also presented in it. As observed from the measured XRD patterns shown in Fig. 2b, the XRD pattern of the precursor WS_2 film shows no detectable diffraction peaks, indicating it is close to amorphous state. However, three diffraction peaks located at 14.31°, 29.02° and 43.74°, are observed from the annealed WS_2 film, corresponding to the (002), (004) and (006) crystal planes of hexagonal WS_2, respectively, confirming the well layer stacking along the c direction.

Figure 2c shows a three-dimensional atomic force microscope (AFM) surface topography scan of the annealed WS_2 film, showing a little edge of the film, mainly because of the cluster effect at the edge during the sputtering and annealing process[9]. Figure 2d presents the section height profile of the WS_2 film located at the marked position in Fig. 2c, confirming the thickness of the annealed WS_2 film at about ~25.2 nm.

Figure 3a,b shows the TEM images of WS_2 at different magnifications, revealing that the WS_2 film is composed of countless WS_2 nanosheets, most of which are horizontal, and few of them are vertically grown. Figure 3c is the SAED pattern of the WS_2 nanosheets, the diffraction rings from inside to outside are ascribed to the (002), (100), (006), (110), (200) planes, respectively, as marked in the figure[24,28]. Figure 3d gives the HRTEM image of the vertically grown WS_2 nanosheets, showing the 0.62 nm interlayer distance of WS_2, identical to the theoretical interlayer distance along the c-axis direction[29]. Figure 3e displays that the HRTEM image of the horizontally

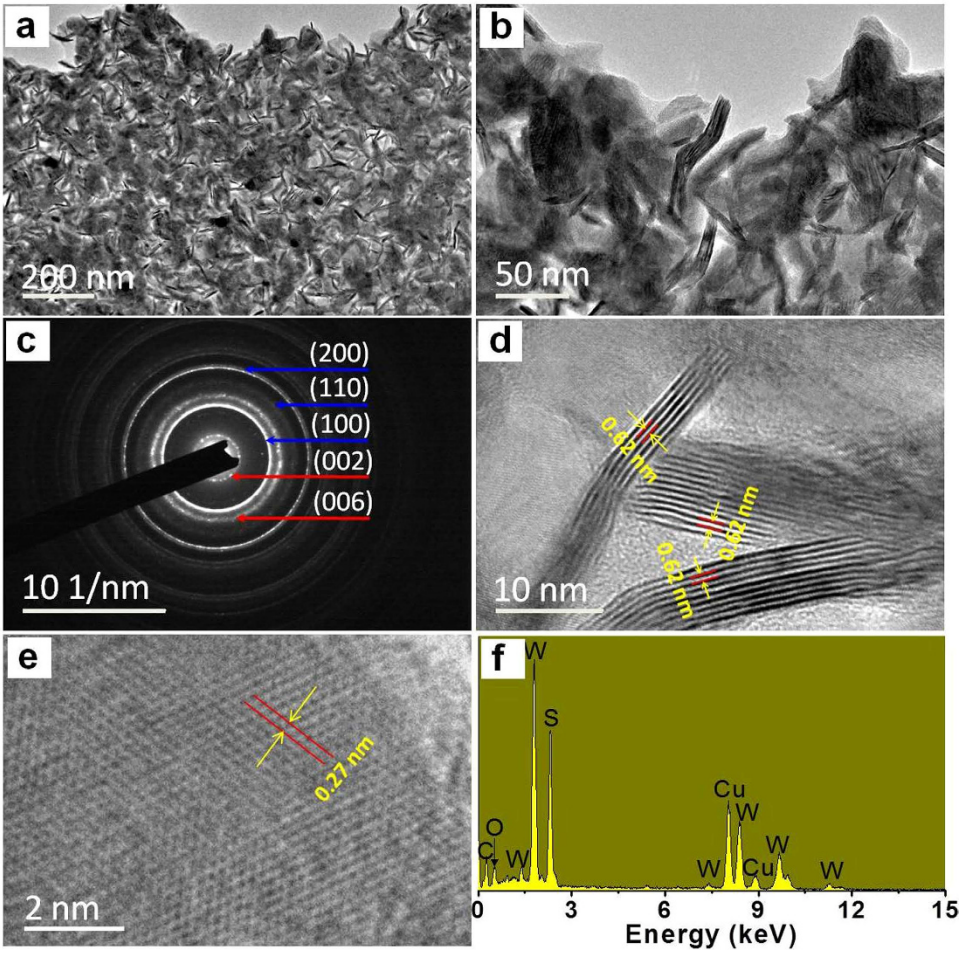

Figure 3. TEM image and analysis of WS_2 film. (**a,b**) TEM images of transferred WS_2 on the carbon-coated copper net. (**c**) The SAED pattern of the WS_2. (**d**) HRTEM image of the vertically grown WS_2 nanosheets. (**e**) HRTEM image of the horizontally grown WS_2 nanosheets. (**f**) EDS spectrum of the sample.

grown WS_2, with 0.27 nm interplane spacing, matches well with the (110) planes, indicating a top view through the c-axis direction[30]. The EDS spectrum of the sample shown in Fig. 3f confirms the tungsten (W) and sulphur (S) elements are contained in the prepared sample, the existence of carbon (C), oxygen (O) and copper (Cu) are due to the carbon-coated copper substrate for TEM measurement.

Discussion

Figure 4a schematically illustrates the fabricated photodetector based on the annealed WS_2 film. The Ti (5 nm)/Au (50 nm) electrodes were deposited on top of the WS_2 film by thermal evaporation method. A stainless steel shadow mask was used to pattern these electrode pads spaced 100 micrometers apart, and the Ti/Au contacts were captured by a CCD microscope and presented in the inset of the Fig. 4b, the photodetector was attached to a chip carrier fixture for electrical testing. Figure 4b shows the current-voltage curve of the annealed WS_2 film measured in absence of light. The quasi-linear and symmetric for small bias voltages indicates ohmic contact between the WS_2 channel and the Ti/Au electrodes. Then, the resistance at room temperature was calculated to be 4.2 kΩ according to the I-V curve shown in Fig. 4b, lower than other ones listed in Table 1, suggesting high quality, conductivity and uniformity of the as-prepared WS_2 film.

To further reveal the photoelectrical response properties of the WS_2 based photodetector, the bias voltage dependent photocurrent of the photodetector at 365 nm was measured and given in Fig. 4c, showing a series of I-V curves under increasing incident light intensity (from 12.1 to 395 $\mu W/cm^2$), from which one can see the highly linear photocurrent of device depending on the bias voltage, indicating the ohmic-like contact between the WS_2 channel and the Ti/Au electrodes. As seen from Fig. 4c,d both the photocurrent and responsivity increase with the applied voltage. Under higher bias voltage, the photo-generated electron-hole pairs can be more effectively separated and captured, with the increase in the carrier drift velocity and then the reduction in carrier transfer time T_t (defined as $T_t = l^2/\mu V$, where l is the device channel length, μ is the carrier mobility and V is the bias voltage)[31], finally resulting in the higher photocurrent and responsivity.

Figure 5a shows the photocurrent of the detector increases linearly with the incident excitation light intensity at the wavelength of 365 nm under various applied voltages. Under higher illumination intensity, more electro-hole pairs are generated in WS_2, with the electrons and holes being directed into different electrodes

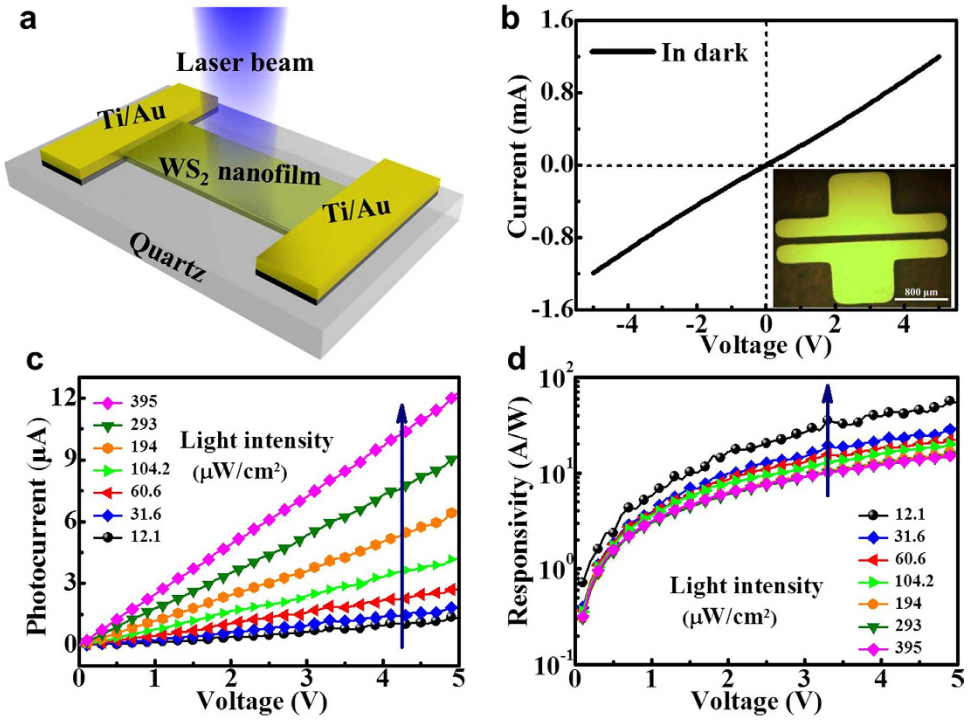

Figure 4. Device structure and photoresponse of photodetector. (**a**) Schematic representation of the photodetector consisting of a WS_2 film and the Ti/Au contacts on quartz, and the laser sources were applied perpendicularly to the film. (**b**) Current-voltage plot obtained without illumination, the inset displays the microscope image of a pair of the Ti/Au electrodes. (**c**) I-V curves of the device obtained under different light intensities from 12.1 to 395 μW/cm^2 at a wavelength of 365 nm. (**d**) The corresponding responsivity *vs.* voltage plots acquired under various light intensities.

Materials	Fabrication Methods	Resistance	Responsivity[b]	Detectivity (Jones)[b]
Multilayer WS_2[a]	Magnetron Sputtering	4.2 kΩ	53.3 A/W	~10^{11}
Few-layer WS_2[10]	CVD	~3 MΩ	92 μA/W	N/A
WS_2 nanoflakes[15]	Mechanical Exfoliation	~4 MΩ	~20 A/W	N/A
Multilayer MoS_2[12]	Magnetron Sputtering	N/A	~300 mA/W	~10^{13}
Multilayer MoS_2[35]	Mechanical Exfoliation	N/A	120 mA/W	~10^{10}
Few-layer MoS_2[9]	Thermolysis	N/A	700 mA/W	~10^{10}
Graphene-MoS_2 hybrid[36]	CVD	2.4 kΩ	62 A/W	N/A
Few-layer InSe[37]	Mechanical Exfoliation	~500 MΩ	~12 A/W	~10^{11}

Table 1. Summary of important device performance parameters of this work and other reported 2D layered transition metal dichalcogenides. [a]This work. [b]Maximum value reported on the experimental data.

guided by the applied electric field, resulting in the increase of the channel photocurrent. As shown in Fig. 5b, however, the responsivity of the photodetector reduced with increasing light intensity. This phenomenon should be attributed to the trap states containing defects and charged impurities within the WS_2 film and at the interface between the quartz and WS_2. Under low light intensity, the photo-generated electrons are mostly captured by the trap states and thus reduce the recombination of the electron-hole pairs. While under high illumination intensity, a relatively lower ratio of the photo-generated electrons will be captured because of the limited quantity of the trap states[31]. Thus, the device was more sensitive under lower light intensity[32].

To analyze the quantitative dependence of the photocurrent on the illumination intensity, the photocurrent measured at $V = 5$ V as a function of light intensity is shown in Fig. 5c. The dependence of photocurrent on light intensity can be fitted by a simple power law: $I_{ph} = AP^{\alpha}$, where I_{ph} is the photocurrent, A is a scaling constant, P is the light power, and α is an exponent. The power equation fits (dashed lines) to the experimental data (solid squares) with an exponent ($\alpha = 0.79$) between 0.5 and 1, indicating that the saturation is attributed to a kinetics of the photo-generated carriers that involves both recombination states and carrier-carrier interactions. The responsivity (R) is defined as the photocurrent generated per unit power of the incident light on the effective area and was obtained from the experimental data by using the formal $R = I_{ph}/P$, and a quantitative fitting of the data yields a power law behavior $R = AP^{\alpha-1}$ with the fitting parameter $\alpha = 0.79$ ($R \propto P^{-0.21}$) (see Fig. 5c).

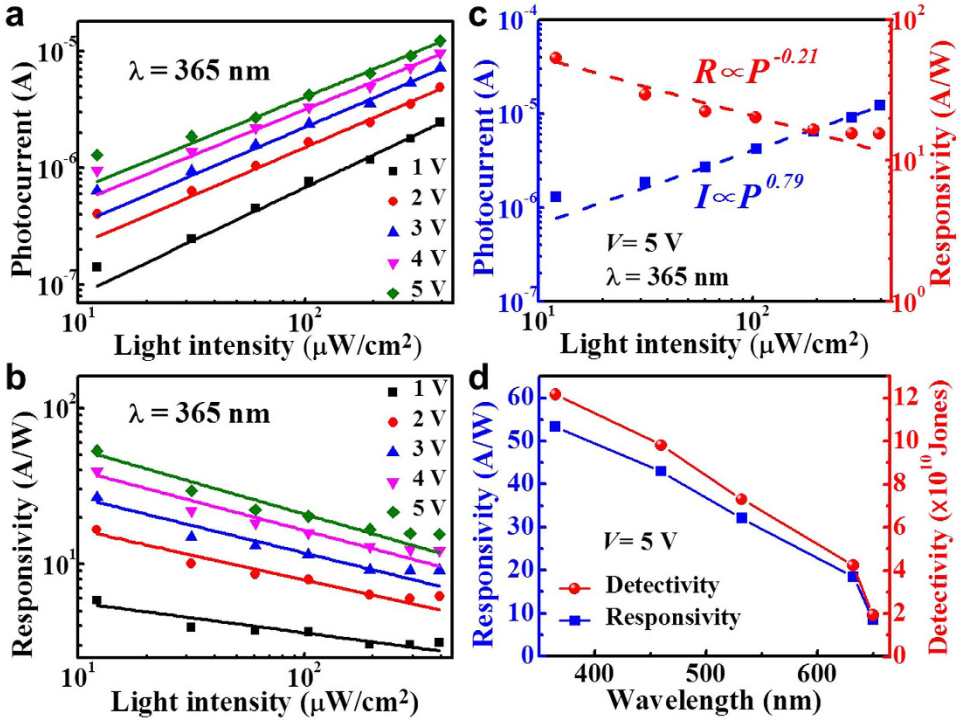

Figure 5. The performance of WS_2 film as photodetector. (**a**) Photocurrent *vs.* light intensity and (**b**) Responsivity *vs.* light intensity plots acquired at different voltages varying from 1 to 5 V. (**c**) Photocurrent and responsivity as functions of light intensity at a 5 V bias voltage. The curves are fitted according to the power law $I_{ph} = AP^{\alpha}$. (**d**) Responsivity and photo-detectivity dependence on wavelength obtained at a 5 V bias voltage.

The photocurrent responses of the device in the visible range are also measured and Fig. 5d depicts the calculated responsivity dependence on the wavelength, showing the responsivity of the WS_2 photodetector increases at shorter spectral wavelengths. This is different from the common GaAs based photodetector of which the responsivity drops at reduced wavelength regions. The results also show the responsivity in the visible range are tens of A/W, much higher than the previously demonstrated records by using few-layered WS_2 films based photodetectors (2.0~92μA/W)[10], implying the capability of WS_2 film based photodetector for conducting broadband photo-detection from the ultraviolet to visible region with promising high responsivity and its suitability for ultraviolet ultrasensitive photodetection. Moreover, to determine the sensibility of detecting a weak optical signal, the specific detectivity (D^*) is measured and calculated. By assuming that shot noise from dark current constitutes a major contribution to the total noise, D^* can be expressed in the form of $D^* = A^{1/2}R/(2qI_{dark})^{1/2}$, where R is the responsivity, A is the effective area of the detector, q is the absolute value of electron charge, and I_{dark} is the dark current[33]. The D^* is calculated to be 1.22×10^{11} Jones at a luminescent light intensity of 12.1 μW/cm^2 at 365 nm and a bias voltage of 5 V. These results are superior or comparable to the previously reported photodetectors that are fabricated on the basis of 2D TMDs, as listed in Table 1. The wavelength dependent responsivity and detectivity of the device displayed in Fig. 5d clearly indicates better responsivity and detectivity at shorter wavelength regions (higher energy side).

In summary, we demonstrate a high performance UV-Vis broadband responsive photodetectors on the basis of low resistance large area WS_2 film fabricated through magnetron sputtering and post-annealing process. The responsivity and detectivity of the photodetector can reach 53.3 A/W and 1.22×10^{11} Jones, respectively. Our results indicate that the magnetron sputtering method is a simple and scalable method for fabricating high quality WS_2 films with diverse device applications, including photodetectors, solar cells, photoelectrochemical cells, phototransistor sensors and so on.

Methods

WS_2 Film and Photodetector Fabrication. WS_2 films on quartz substrate were produced by magnetron sputtering method followed by post annealing. The WS_2 precursor film was first deposited on clean quartz substrate through sputtering by using sintered WS_2 disks (Φ_2*0.125 inch) bought from China New Metal Materials Technology Co, Ltd. as the target. The radio frequency (RF) power, argon gas pressure, and quartz substrate temperature were set to be 60 W, 50 Pa, and 200 °C, respectively, for the fabrication process. The deposition rate was about 5 nm min^{-1}, leading to a 25.2 nm thick WS_2 film after a deposition time of 5 min. The post annealing process was then carried out to enhance the crystallinity of the WS_2 film. The WS_2precursor film on quartz was loaded in a tubular reactor, and with sulfur powder (99.5% purity) being placed upstream in the chamber as shown in Fig. 1a. Sulfur was evaporated at 200 °C dragged by 100 sccm Argon flow. The center temperature of the tube furnace was set to 800 °C and kept stable for 2 hours, followed by being cooled down to room temperature

naturally so as to complete the annealing processes. In fact, the post-annealing process can be done within the sputtering chamber by directly heating the substrate to high temperature under H_2S atmosphere during the sputtering process[34]. The Ti/Au electrodes were deposited on top of the WS_2 film by thermal evaporation using a stainless steel shadow mask to form channels (Width/Length = 2 mm/0.1 mm) for the electrical and photoelectrical measurements.

Characterizations of Materials and Devices. UV-Vis absorption and transmission spectra were recorded on a SHIMADZU UV-2550 UV-Vis spectrophotometer. The Raman spectra measurements were carried out on a HR-800 Raman spectrometer with a 488 nm argon ion laser. The X-ray diffraction (XRD) pattern was recorded using a RigakuSmartLab X-ray diffractometer. The surface morphology and height information of samples were obtained by atomic force microscopy (AFM, VeecoNanoscope V).The morphology, crystal structure and chemical composition were investigated using a field emission transmission electron microscope (FETEM, JEOL Model JEM-2100F), equipped with an energy dispersive spectrometer (EDS). Additionally, to evaluate the photoresponse performance of the as-prepared WS_2 film based photodetector, five laser sources operating at different wavelengths (365 nm, 460 nm, 532 nm, 632 nm and 650 nm) were used for the measurements. Electrical measurements were performed on a semiconductor characterization system (Keithley 2400-SCS).

References

1. Geim, A. K. Graphene: Status and Prospects. *Science.* **324,** 1530–1534 (2009).
2. Geim, A. K. & Novoselov, K. S. The Rise of Graphene. *Nat. Mater.* **6,** 183–191 (2007).
3. Bonaccorso, F., Sun, Z., Hasan, T. & Ferrari, A. C. Graphene Photonics and Optoelectronics. *Nat. Photonics* **4,** 611–622 (2010).
4. Sun, Z.*et al.* Infrared Photodetectors Based on CVD-Grown Graphene and PbS Quantum Dots with Ultrahigh Responsivity. *Adv. Mater.* **24,** 5878–5883 (2012).
5. Wang, Y., Qu, Z., Liu, J.& Tsang, Y. H. Graphene Oxide Absorbers for Watt-Level High-Power Passive Mode-Locked Nd:$GdVO_4$ Laser Operating at 1 Mm. *J. Light. Technol.* **30,** 3259–3262 (2012).
6. Luo, L. B. *et al.* Near-Infrared Light Photovoltaic Detector Based on GaAs Nanocone Array/monolayer Graphene Schottky Junction. *Adv. Funct. Mater.* **24,** 2794–2800 (2014).
7. Zhao, Y. *et al.* Mass Transport Mechanism of Cu Species at the Metal/Dielectric Interfaces with a Graphene Barrier. *ACS Nano* **8,** 12601–12611(2014).
8. Zhao, J. Q. *et al.* L-Band Graphene-Oxide Mode-Locked Fiber Laser Delivering Bright and Dark Pulses. *Laser Phys.* **23,** 075105 (2013).
9. Tsai, D. S. *et al.* Few Layer MoS_2 with Broadband High Photogain and Fast Optical Switching for Use in Harsh Environments. *ACS Nano* **7,** 3905–3911(2013).
10. Perea-Lopez, N. *et al.* Photosensor Device Based on Few-Layered WS_2 Films. *Adv. Funct. Mater.* **23,** 5511–5517 (2013).
11. Georgiou, T. *et al.* Vertical Field-Effect Transistor Based on Graphene-WS_2 Heterostructures for Flexible and Transparent Electronics. *Nat. Nanotechnol.* **8,** 100–103 (2013).
12. Wang, L. *et al.* MoS_2/Si Heterojunction with Vertically Standing Layered Structure for Ultrafast, High-Detectivity, Self-Driven Visible-Near Infrared Photodetectors. *Adv. Funct. Mater.* **25,** 2910–2919 (2015).
13. Radisavljevic, B., Radenovic, A., Brivio, J., Giacometti, V. & Kis, A. Single-Layer MoS_2 Transistors. *Nat. Nanotechnol.* **6,** 147–150 (2011).
14. Gong, Y. *et al.* Vertical and in-Plane Heterostructures from WS_2/MoS_2 Monolayers. *Nat. Mater.* **13,** 1135–1142 (2014).
15. Huo, N. *et al.* Photoresponsive and Gas Sensing Field-Effect Transistors Based on Multilayer WS_2 Nanoflakes. *Sci. Rep*. **4,** 5209 (2014).
16. Kuc, A., Zibouche, N. & Heine, T. Influence of Quantum Confinement on the Electronic Structure of the Transition Metal Sulfide TS_2. *Phys. Rev. B* **83,** 245213 (2011).
17. Bernardi, M., Palummo, M. & Grossman, J. C. Photovoltaics Using Two-Dimensional Monolayer Materials Extraordinary Sunlight Absorption and one Nanometer Thick Photovoltaics Using Two-Dimensional Monolayer Materials. *Nano Lett.* **13,** 3664–3670 (2013).
18. Brivio, J., Alexander, D. T. L. & Kis, A. Ripples and Layers in Ultrathin MoS_2 Membranes. *Nano Lett.* **11,** 5148–5153 (2011).
19. Eda, G., Yamaguchi, H., Voiry, D., Fujita, T., Chen, M. & Chhowalla, M. Photoluminescence from Chemically Exfoliated MoS_2. *Nano Lett.* **11,** 5111–5116 (2011).
20. Li, H., Wu, J., Yin, Z. & Zhang, H. Preparation and Applications of Mechanically Exfoliated Single-Layer and Multilayer MoS_2 and WSe_2 Nanosheets. *Acc. Chem. Res.* **47,** 1067–1075 (2014).
21. Li, X. *et al.* Large-Area Synthesis of High-Quality and Uniform Graphene Films on Copper Foils. *Science* **324,** 1312–1314 (2009).
22. Schmidt, H. *et al.* Transport Properties of Monolayer MoS_2 Grown by Chemical Vapour Deposition. *Nano Lett.* **14,** 1909–1913 (2014).
23. Wang, X. *et al.* Chemical Vapor Deposition Growth of Crystalline Monolayer $MoSe_2$. *ACS Nano* **8,** 5125–5131 (2014).
24. Zhang, Y. *et al.* Controlled growth of high-quality monolayer WS_2 layers on sapphire and imaging its grain boundary. *ACS Nano* **7,** 8963–8971 (2013).
25. Zhao, W. *et al.* Lattice Dynamics in Mono- and Few-Layer Sheets of WS_2 and WSe_2. *Nanoscale* **5,** 9677–9683 (2013).
26. Zhu, B., Chen, X. & Cui, X. Exciton Binding Energy of Monolayer WS_2. *Sci. Rep.* **5,** 9218 (2014).
27. Berkdemir, A. *et al.* Identification of Individual and Few Layers of WS_2 Using Raman Spectroscopy. *Sci. Rep.* **3,** 1755 (2013).
28. Gutie, H. R. *et al.* Extraordinary Room-Temperature Photoluminescence in Triangular WS_2 Monolayers. *Nano Lett.* **13,** 3447–3454 (2013).
29. Late, D. J., Liu, B., Matte, H. S. S. R., Rao, C. N. R. & Dravid, V. P. Rapid Characterization of Ultrathin Layers of Chalcogenides on SiO_2/Si Substrates. *Adv. Funct. Mater.* **22,** 1894–1905 (2012).
30. Du, Y. *et al.* Improving the Anode Performance of WS_2 through a Self-Assembled Double Carbon Coating. *J. Phys. Chem. C* **119,** 15874–15881 (2015).
31. Lopez-Sanchez, O., Lembke, D., Kayci, M., Radenovic, A. & Kis, A. Ultrasensitive Photodetectors Based on Monolayer MoS_2. *Nat. Nanotechnol.* **8,** 497–501 (2013).
32. Konstantatos, G. *et al.* Ultrasensitive Solution-Cast Quantum Dot Photodetectors. *Nature* **442,** 180–183 (2006).
33. Zeng, L. *et al.* Bilayer Graphene Based Surface Passivation Enhanced Nano Structured Self-Powered near-Infrared Photodetector. *Opt. Express* **23,** 4839–4846 (2015).
34. Ellmer, K. Preparation routes based on magnetron sputtering for tungsten disulfide (WS_2) films for thin-film solar cells. *phys. stat. sol. (b)* **245,** 1745–1760, (2008).
35. Choi, W. *et al.* High-Detectivity Multilayer MoS_2 Phototransistors with Spectral Response from Ultraviolet to Infrared. *Adv. Mater.* **24,** 5832–5836 (2012).
36. Xu, H. *et al.* High Responsivity and Gate Tunable Graphene-MoS_2 Hybrid Phototransistor. *Small* **10,** 2300–2306 (2014).
37. Tamalampudi, S. R. *et al.*High Performance and Bendable Few-Layered InSe Photodetectors with Broad Spectral Response. *Nano Lett.* **14,** 2800–2806 (2014).

Acknowledgements
This work is financially supported by the Research Grants Council of Hong Kong, China (Project number: GRF 526511/PolyU B-Q26E), and the Hong Kong Polytechnic University (Project number: 1-ZE14).

Author Contributions
L.H.Z. and L.L.T. planned and performed the experiments, collected and analyzed the data, and wrote the paper. S.P.L. and Y.H.T. supervised the project, and conceived the experiments, analyzed the results and wrote the paper. C.Y.T., B.Z., H.L. and C.Y. helped with synthesis of the materials and collected the data. All authors have discussed the results and read on the manuscript.

Additional Information
Competing financial interests: The authors declare no competing financial interests.

How to cite this article: Zeng, L. *et al.* High-responsivity UV-Vis Photodetector Based on Transferable WS_2 Film Deposited by Magnetron Sputtering. *Sci. Rep.* **6**, 20343; doi: 10.1038/srep20343 (2016).